IMPROVING VALIDATION OF PREDICTIVE TOOLS FOR INJECTOR-COUPLED COMBUSTION INSTABILITIES

Justin S. Hardi (1), Jan Martin (1), Roland Kaess (2), Tim Horchler (3), Stefan Koeglmeier (2), Federica Tonti (1), Sebastian Soller (2), and Andreas Gernoth (4)

(1) Institute of Space Propulsion, DLR, Lampoldshausen, Germany
(2) ArianeGroup GmbH, Ottobrunn, Germany
(3) Institute of Aerodynamics and Flow Technology, DLR, Göttingen, Germany
(4) ESA, ESTEC, Noordwijk, The Netherlands

ABSTRACT

This paper summarises work conducted within an ESA TDE project addressing the development of predictive tools for the avoidance of injector-coupled combustion instabilities during the design phase of cryogenic rocket engines. A new experimental combustion chamber was operated for the first time to generate validation data for numerical tools. The chamber was operated at pressures from 40 to 70 bar, at load points both sub- and supercritical for oxygen. The single injection element is representative of those found in number in lower stage engines in terms of dimension and propellant flow rate. Tests have been performed in the frame of the current project with LOX and hydrogen at cryogenic temperatures. The chamber is well instrumented with pressure and temperature sensors, and extraordinarily large optical access windows facilitate the application of high-speed visualisation techniques to resolve the spatial and temporal response of the flame. Achieved experimental conditions were modelled to benchmark existing numerical tools. Different modelling approaches were compared, including the industrial state-of-the-art in hybrid combination of lower order methods, and unsteady CFD of the reacting flow field. While the hybrid approach is efficient and fast with acceptable accuracy for design purposes, CFD allowed the nature of the coupled modes to be studied in detail, and the dynamic flame response to be predicted.

Index Terms— liquid propellant rocket engine, cryogenic propellants, combustion instability, acoustics

1. INTRODUCTION

Combustion instabilities are acoustic waves driven to damagingly high amplitude by the coupling with energy release from combustion. The phenomenon remains a difficult hurdle in the development of liquid propellant rocket engines. It is therefore desirable to develop numerical tools for predicting potential coupling between acoustic modes of the combustion chamber and of the injectors for cryogenic propellants like LOX/H_2 or LOX/LNG.

While generally considered to have good stability characteristics, engines using the propellant combination liquid oxygen/hydrogen (LOX/H_2) with shear coaxial injectors are not immune to the problem [1] [2] [3] [4]. In the 1960s one of the main parameters to assess the risk of combustion instabilities within LOX/H_2 combustion chambers was the H_2 temperature. Within several experimental investigations, in which the inlet temperature of H_2 was varied between cryogenic and ambient temperatures, the dependence of instability onset at low H_2 temperatures was found to be related to several geometrical and operational parameters [5] [6] [7] [5] [8] [9] [10] [11] [12] [13].

Two of the few modern studies into the influence of H_2 temperature on stability have been performed by Astrium and the German Aerospace Center (DLR). In 2011, Astrium (now ArianeGroup GmbH, Ottobrunn) performed tests with a subscale combustor under operating conditions representative of industrial engines, and recreated conditions under which spontaneous instability was expected to occur [14]. Specifically, the hydrogen injection temperature was reduced continuously in the hopes of observing an instability onset event of the variety reported extensively in literature from the 1960s-1970s. No cases of high frequency combustion instability were experienced with either of the two element types tested in the Astrium combustor. Analysis of dynamic pressure measurements collected from the DLR-designed measurement ring revealed unexpected trends in combustion roughness with varying H_2 temperature. Combustion roughness generally decreased with decreasing H_2 temperature, as seen in Figure 1. Albeit recorded at far lower acoustic amplitudes, this observation is not in line with the consistent increase in unstable behaviour with lowering H_2 temperature noted during extensive NASA testing in the 1960s.

The impact of H_2 temperature on chamber acoustics and acoustic excitation was at the time also the subject of a research program conducted at DLR using the research combustor 'BKD' with a similar configuration to the Astrium sub-scale combustor. The BKD experiences self-excited combustion instability under certain operating conditions with relatively high H_2 temperature, although it should be

stable according to the design criteria established in the 1960s [15] [16]. This outcome showed that unsteady combustion processes in LOX/H$_2$ engines had not yet been fully understood.
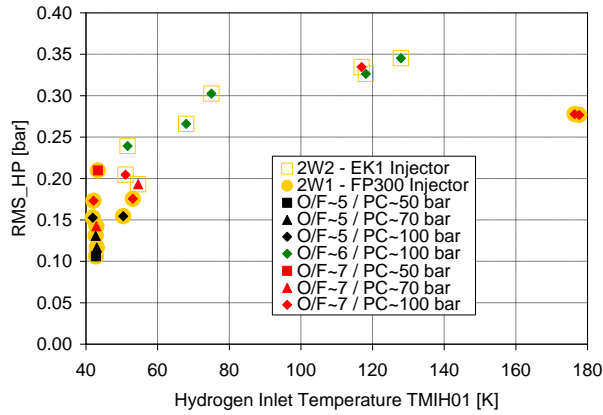
Figure 1. Dependence with H$_2$ temperature of RMS values of dynamic pressure. Dynamic pressure signals are high pass filtered with a cut-off frequency of 1.6 kHz [14].
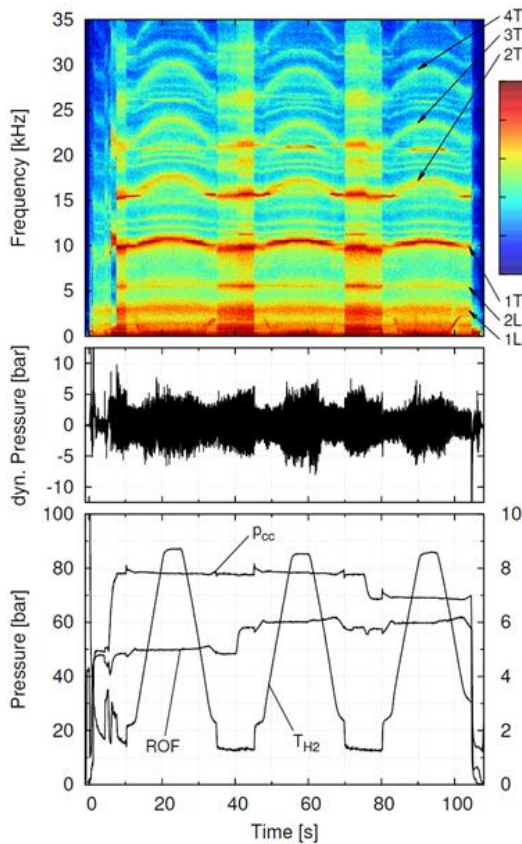
Figure 2. Test sequence and spectrogram of dynamic pressure in the chamber of BKD for a H$_2$ temperature ramping test.
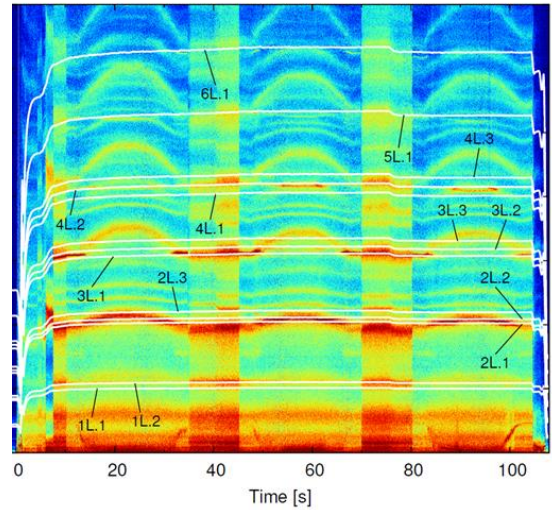
Figure 3: Spectrogram of dynamic pressure in the chamber of BKD, overlaid with the 1T mode frequency and the LOX post frequency measured from the optical probes.

The implementation of optical probes into the combustion chamber to observe unsteady flame radiation helped shed light on the stability behaviour in BKD. Figure 2 shows the data from a test with H$_2$ temperature ramping in BKD. The lower box shows the test sequence with Pcc, ROF and T$_{H2}$, the centre plot shows an unsteady pressure sensor signal, and the upper plot the corresponding spectrogram. The impact of T$_{H2}$ on chamber acoustics is clearly visible as the lines representing the chamber resonance frequencies follow the T$_{H2}$ signal. Figure 3 shows the pressure spectrogram overlaid with the calculated frequency signals of the LOX post resonance mode. These signals were calculated using the results of the measurements with fibre optical probes [16] [17]. The excitation of combustion chamber modes is observed when chamber frequencies match the LOX post frequencies. This data thus represents a rare, direct, and repeatable demonstration of injection coupling in a liquid rocket thrust chamber.

Faced with these data sets, efforts were initiated to develop the capability to predict injector coupling numerically. Tests cases were formulated from the data and modelled using in-house developed tools and methods to attempt to reconcile the stability behaviour of BKD with the observations from the Astrium combustor. Although the numerical tools provided property distributions which were in good agreement with the experimental results, a precise estimation of the chamber and injector frequencies could not be achieved. Injector mode frequencies were generally underestimated and chamber modes overestimated, thus eluding the expected mode matching [18]. The need for improvement of the numerical approaches was identified,

together with the need for a suitable set of experimental data to validate the tools precisely, or to properly identify weaknesses in the tools [19].

The need for validation data led to the development of a new experiment at DLR. The experiment was designed to be capable of verifying the performance of the stability prediction tools, and has three key features. First, the combustor was configured with a single shear coaxial injector and a subscale combustion chamber, operating at conditions relevant to industrial thrust chambers. A single-injector reduces the computational efforts in modelling the test case and also allows unobscured optical access to the flame. Second, the necessity was identified to have a window sized according to the expected penetration length of the intact LOX core into the chamber in order to be able to measure the flame topology. Third, self-excited injection-coupled instabilities should be facilitated.

This article reports on the first tests of the new experiment, using LOX/H$_2$ propellants, and the numerical modelling work that followed. The focus of this project is on studying resonant coupling between injector and combustion chamber. A test case was derived from new data obtained from a test campaign at the European Research and Technology Test Facility P8 for Cryogenic Rocket Engines located at DLR in Lampoldshausen. The test cases were modelled using tools available in house to the partners DLR and ArianeGroup GmbH (AGG). The numerical results of the partners were compared to the experimental data to assess the ability of the partners' tools to predict the coupling of combustion chamber and injector acoustic modes. The tools used by different partners were also cross-compared.

1. EXPERIMENTAL METHOD

The DLR Institute of Space Propulsion has developed an experimental combustor to extend the capabilities of investigating the interaction of LOX/H$_2$ or LOX/CH$_4$ combustion with acoustics and simultaneously provide a detailed set of boundary conditions essential for numerical modelling of these phenomena. Experimental combustor model 'N' (BKN) [20], illustrated in Figure 4, is operated at the P8 test facility. BKN has a circular cross section and aims for the excitation of longitudinal HF instabilities.

The BKN window segment in combination with the BKN windows feature a curved inner surface of the window and hence no discontinuity of the circular inner chamber geometry, as seen in Figure 4. The propellants are injected axially through the injector at the front of the chamber. Optical access to an area extending from the injection plane to a distance shortly before the nozzle contraction section is provided through windows which can be optionally mounted on one or both sides of the chamber.

The injector consists of a single centrally positioned shear-coaxial element providing liquid oxygen as the oxidizer
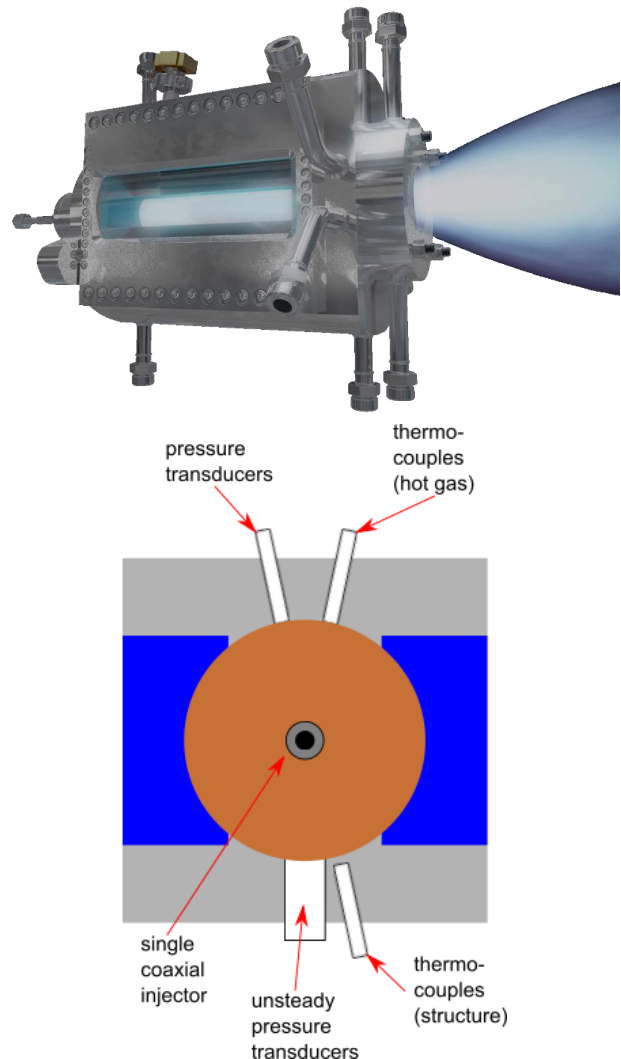
**Figure 4: DLR subscale combustion chamber model 'N' (BKN) with optical access**
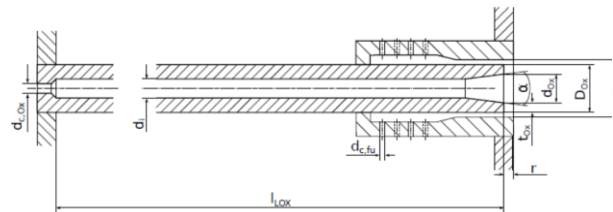
Figure 5: Test case injection element[1]

whilst the fuel is gaseous hydrogen. Key parameters of the injection element with tapering and recess is given in Figure 5 and Table 1. A hydrogen film cooling at ambient temperature is injected through a ring slot located at the outer diameter of the chamber.

Table 1: Geometrical values of injection element

| Description	Symbol	Unit	Value
Inner diameter LOX post	d_i	mm	5,5
Exit diameter LOX post	d_{Ox}	mm	6,3
Outer diameter LOX Post	D_{Ox}	mm	7,2
Outer diameter FUEL annulus	d_{Fu}	mm	8,2
Recess LOX post	r	mm	4,0
Thickness LOX post tip	t_{Ox}	mm	0,45
Angle of taper LOX post	α	°	8,0

Data from several tests was gathered from seven steady-state operating conditions, or load points (LPs). The LPs range combustion chamber pressure (Pcc) values between 40 and 70 bar, and ratio of oxidiser to fuel (ROF) values between 3 and 6.5. The LPs are plotted over the possible operating domain of BKN in Figure 6.
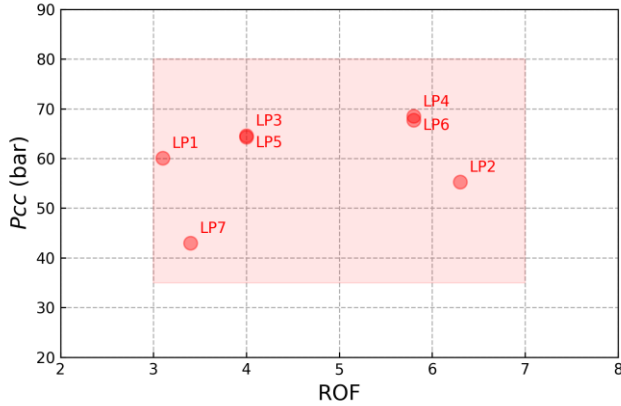
Figure 6: Load points (operating conditions) achieved within the test campaign (red points), and design operating envelope of BKN (pink box).

Two types of flame emission were investigated using high-speed imaging; the ultraviolet (UV) and the visible (blue) regimes. Visualization of the UV and blue regimes was carried out using two synchronously and coaxially recording high-speed camera systems, shown schematically in Figure 7. While the source of the filtered UV radiation is the excited hydroxyl radical (OH*), OH* radiation suffers from high self-absorption and thermal excitation at usual operating conditions in rocket combustors [21]. This explains the differences in character between OH* and blue radiation imaging of shear coaxial LOX/H$_2$ flames [22].

Imaging of each LP was recorded with frame rates of either 3 or 50 kfps. Some images with the large and new window are overexposed to a certain extent. The overexposure was due to the first operation of BKN with the Full-Length Optical Window (FLOW), which transmitted more intensity than expected and for which there were no experience-based settings for the camera parameters.
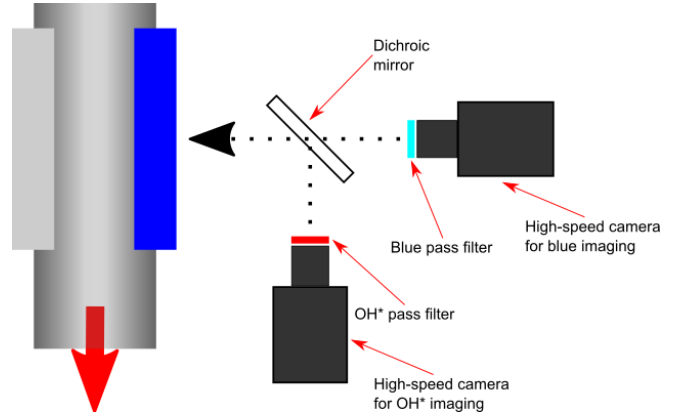

Figure 7: Principal scheme of the optical diagnostic setup at the test facility P8

2. EXPERIMENTAL RESULTS
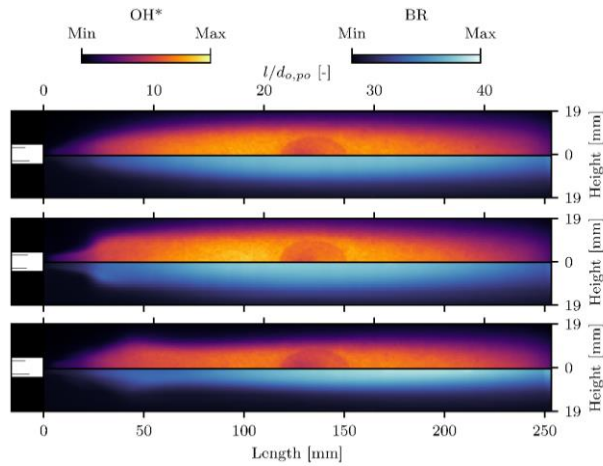
2.1. Flame characteristics

Figure 8 shows the first frame recorded by the high-speed camera systems within the time windows of LP5, LP5 and LP6, respectively. All three images reveal the highly turbulent flame structure for the supercritical LOX/hydrogen combustion.
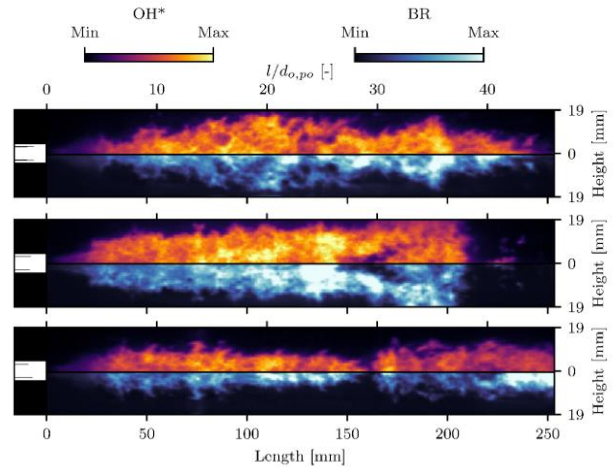
Figure 8: Single frame of OH* (top half) and blue radiation (bottom half) of LP5 (top), LP6 (middle), LP7 (bottom)

Figure 9 shows time-averaged images over the whole duration of LP5, LP6 and LP7, respectively. Generally, OH* emissions and radiation in the blue regime seem to be quite similar. These Figures can be used for a qualitative comparison between simulation and experiment. A significant difference in LP6 compared to LP5 is the

formation of a shoulder-like structure in the near-injector region, at an axial location of around 20-30 mm.


Figure 9: Time averaged image of OH* (top half) and blue radiation (bottom half) of LP5 (top), LP6 (middle), LP7 (bottom)

Certain geometrical flame characteristics such as opening angle, flame width and height can be used for first comparison between experiment and numerical modelling. The mean images of all LPs provide the best opportunity to extract those flame characteristics. Figure 10 illustrates the detected flame boundaries for LP1, the binarized image and the extracted flame angle. For all LPs time averaged images of the OH* radiation were used because steeper intensity gradients in the flame boundary regions result in improved flame boundary detection. Time averaging of the mean images was performed over 0.5 s. Figure 10 also reveals an artefact in the OH* images (indicated by blue ellipse) caused by damage to the intensifier from a previous test campaign. The artefact expresses itself in a local, unphysical area of reduced intensity and has been excluded from the data analysis.

As mentioned before, OH* images for LP3 and LP4 the are overexposed to a large extent. However, this does not hinder the measurement of flame opening angle as performed here. For the flame width, mean values of each column were calculated. In this case, 75% of the peak mean image intensity was used to define the flame width at half maximum (FlW34M) and the flame length at half maximum (FlL34M). It should be noted that for the latter case only the downstream limitation of the intensity at half maximum has been considered.

The results for flame opening angle are summarized in Figure 11 where they are plotted against momentum flux ratio (J). These values follow the expected trend, which is an increasing flame opening angle for higher J values due to greater shear forces leading to accelerated mixing [23]. A

logarithmic trendlines has been added to Figure 11 for orientation only.
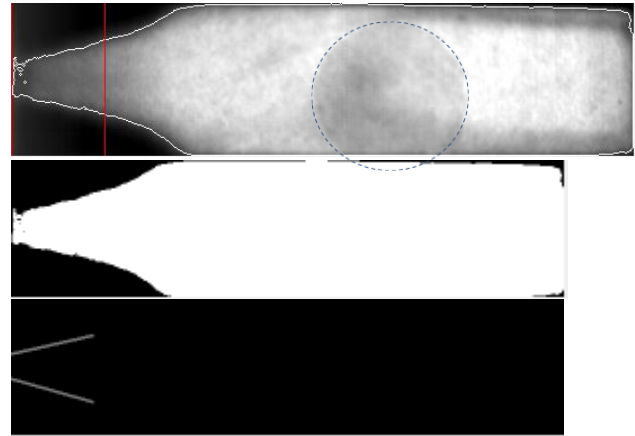
Figure 10: Time averaged OH* radiation image with detected flame (top), binarized image of the detected flame (bottom left) and the extracted flame boundaries in the region of interest (defined by red rectangle)
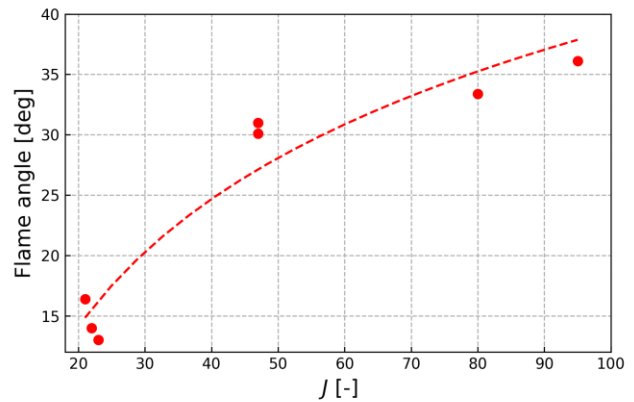
**Figure 11: Flame opening angle vs momentum flux ratio (J)**

2.2. Acoustic stability

In order to determine the extent of injection coupling within the tests conducted in this project, the unsteady pressure was analysed. Figure 12 shows a spectrogram from the flush-mounted high-frequency pressure sensor nearest the injection plane. White lines indicate the resonance frequency of the LOX post, calculated from the measured thermodynamic state of the LOX entering the injector. The horizontal yellow lines correspond to the longitudinal modes of the combustion chamber at ~2400, 4800, and 7200 Hz. The LOX post modes do not intersect the combustion chamber modes during the test, and the chamber modes are of so there is no evidence of excitation arising from LOX-post coupling.

Furthermore, the calculated frequency of the first longitudinal LOX post resonance frequency is not within the expected whistling range. According to Equation 1, the expected whistling frequency is dependent on fluid velocity ($u_{orifice}$), length of the orifice ($l_{orifice}$), and is known to occur in the range of Strouhal-numbers between 0.2 and 0.4.

$$St = \frac{f_{whistling} \cdot \text{l}_{\text{orifice}}}{u_{orifice}} \qquad \text{Equation 1}$$

A confluence of combustion chamber mode frequencies, LOX-post mode frequencies, and LOX orifice whistling frequencies would be expected to result in heightened acoustic excitation in the combustion chamber [24].
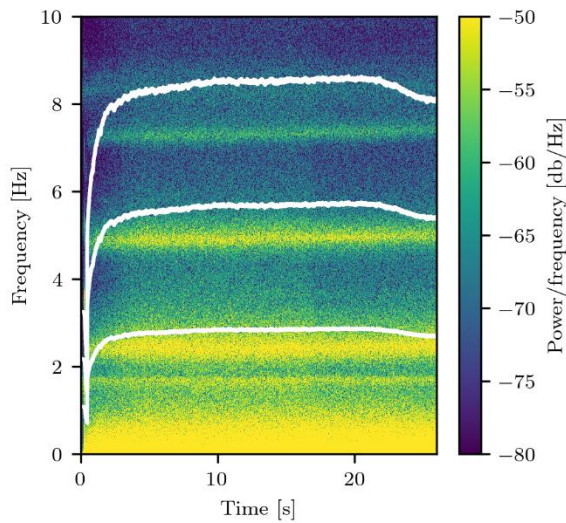

Figure 12: Spectrogram of unsteady pressure sensor in combustion chamber, overlaid with calculated LOX-post resonance frequencies (white lines)

2.3. Flame dynamics

The lack of high amplitude acoustic excitation motivated an analysis of flame dynamics from the high-speed optical data. Dynamic mode decomposition (DMD) is a dimensionality reduction algorithm developed by Schmid [25]. This algorithm computes a set of modes which are associated with a fixed oscillation frequency and growth rate. Following Beinke [26] this approach can be extended to decompose the sensor signals as well.

Figure 13 illustrates a sequence of high-speed images in the blue regime decomposed by the DMD algorithm and reconstructed at a frequency of 2400 Hz, corresponding to the first longitudinal frequency of the chamber. The phase of the snapshots with respect to the unsteady pressure at the faceplate is given below each reconstruction. During a moment of increased pressure, the combustion products accumulate as indicated by the red box in the top left image.

While the pressure decreases these are propagated downstream before a radial spread structure is formed again with increasing pressure. The radial stretching may be caused by a longitudinal compression. This process occurs periodically as is visible in the flame shape of all three reconstructed snapshots. The snapshots further indicate alternating regions of increased and decreased intensity, probably resulting from mass flow modulation due to the acoustic pressure oscillations at the head end of the chamber.
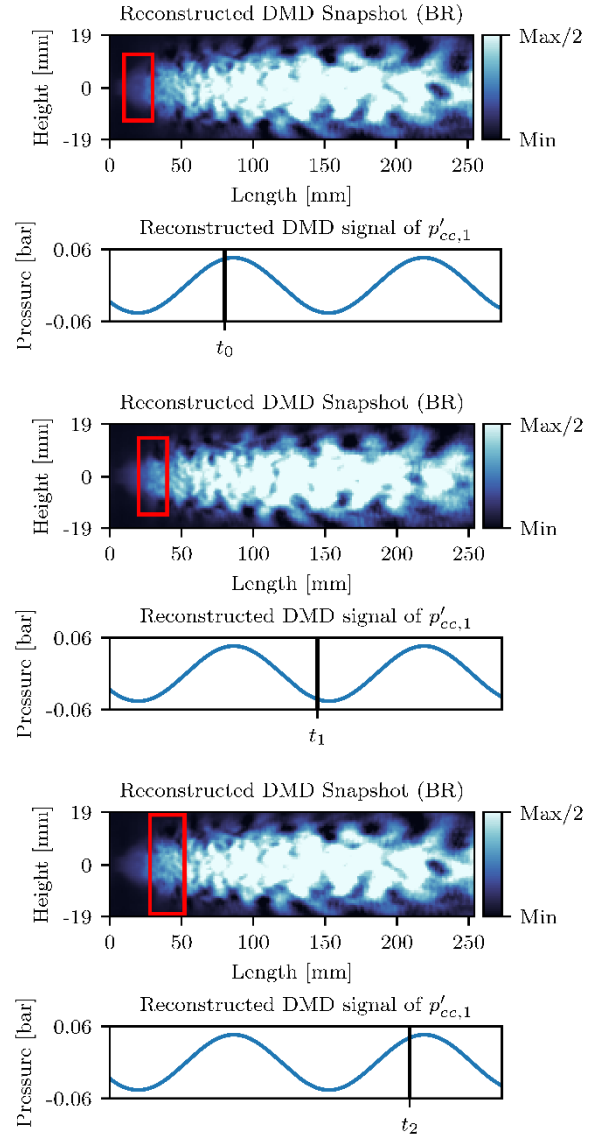
Figure 13: Sequence of reconstructed snapshots filtered at a frequency of 2400 Hz for LP5.

Figure 14 provides a decomposed and reconstructed snapshot from a similar sequence from the same LP but at a frequency of 2680 Hz. At this frequency the first longitudinal

resonance frequency of the LOX post is expected. During an instant of decreased pressure, a wider opening angle occurs. With increasing pressure, the opening angle decreases. This results in a pulsating structure very similar to that at 2400 Hz in Figure 13. It should be noted here, that the energy in both DMD modes was relatively small, yet clear and independent dynamical flame responses could be identified and isolated at frequencies corresponding to two acoustic systems; the combustion chamber and the injector. The frequency spacing between these modes confirms the lack of injector-coupling in the experiment, so it is not surprising that no evidence of LOX post coupling was evident in the unsteady pressure measurements. However, despite unmatched frequencies and a possible lack of additional excitation of the LOX post dynamics by orifice whistling, both effects were active, which underlines the potential threat of injection-coupled instabilities if the frequency spacing between both effects becomes small.
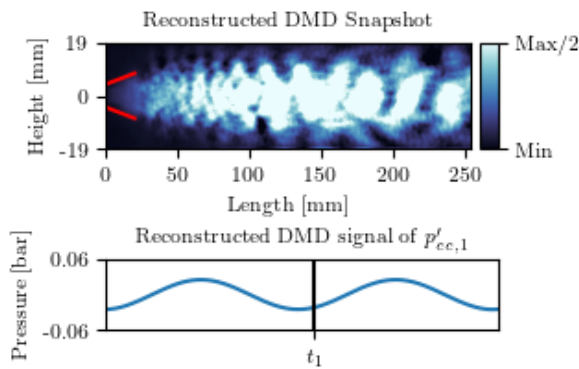
Figure 14: Reconstructed snapshot filtered at a frequency of 2680 Hz for LP5.

3. NUMERICAL MODELLING

The first four of the seven LPs in the experiment were formulated into a test case for numerical modelling within the scope of the project. The partners used two different modelling approaches which are summarised in this section.

3.1. Hybrid CFD-CAA approach

The approach to model the test cases at AGG is known as a hybrid approach because the flow field and acoustic calculations in the combustion chamber are separated, and two different approaches for modelling the combustion chamber and the LOX post are used.

For the combustion chamber, the single injector CFD model was calculated on a full-3D domain in the commercial solver CFX. The flow field solution was interpolated onto a 3D chamber domain for the chamber in the in-house acoustic solver PIANO. The linearized Euler equations were solved in

the time domain after applying a Gaussian pulse excitation source to the chamber. The data were evaluated at different locations in the domain using FFT. This process is illustrated in Figure 15.
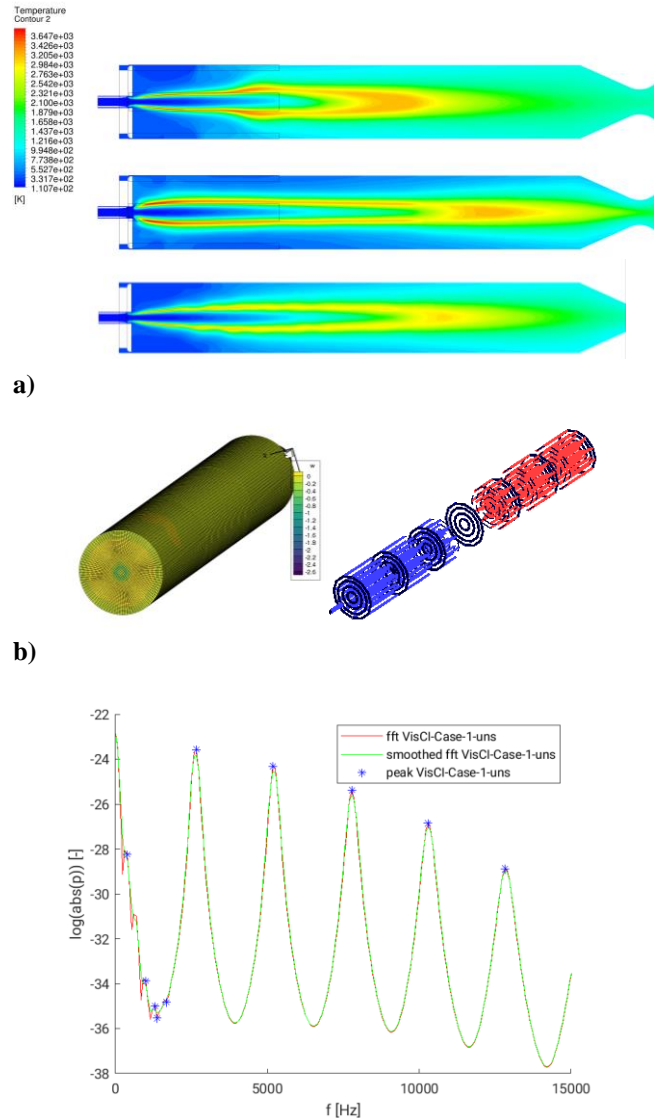
Figure 15. AGG approach to predicting injector coupling; (a) CFX single injector solutions for LP1, LP2, and LP3, (b) 3D PIANO domain of combustion chamber (left) and example pressure field of 1L mode (right), (c) example resonance spectrum result from PIANO calculation.

In parallel, a 1D acoustic network model of the LOX injector was constructed in Matlab. The equations used are typical for 1-D acoustics in the frequency domain, for example the acoustic transmission through a duct, or the transmission through changes in cross section of ducts. For

each acoustic element, the acoustic quantities u' and p' at its upstream and downstream end are connected via a set of equations. The values at the downstream end of element n then correspond to the upstream values of the following element n+1. In this way, a set of equations can be constructed describing the entire system. The outlet of the injector was forced acoustically with a frequency sweep and the resulting response spectrum was inspected to identify resonance frequencies. An example result for LP3 is shown in Figure 16. These frequencies were then compared to the frequencies of the chamber modes identified from the PIANO results.
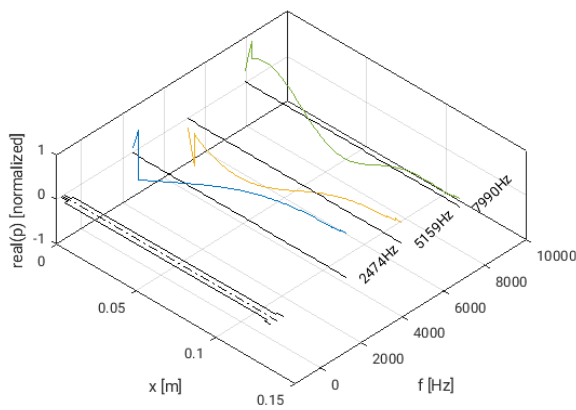
Figure 16: LOX-post eigenfrequencies and mode shapes from the 1D injector acoustic network model for LP3.

3.2. Hybrid CFD-CAA results

The mean flow fields of the CFD calculations were compared to the data from BKN. Combustion chamber wall pressure measurements are compared in Figure 17, by way of example for LP3 with an operating condition of 64 bar at ROF 4. The CFD results have a systematic over-estimation of the pressure of about 5 bar. The reason may be the simplified combustion model (2 reactions for the combustion, 1 for the phase change of LOX to GOX).

The temperature distributions for LP3 are shown Figure 18. The data in the simulation was averaged over the wall surface at the corresponding axial position. The range of values from CFD and measurements compare well, also there are deviations in the profile which may reflect local effects arising from the interaction of the hot gas and the cooling film. The wall resolution in the simulation was not very fine as the focus was more on the flame shape. Also, there could be local effects in the measurements or effects of axial heat conduction in the solid.

The predicted mode frequencies for LPs 1-3 in the combustion chamber are compared with experimental values

in Table 2. The agreement with experiment is very good on the chamber side for LP2 and LP3.
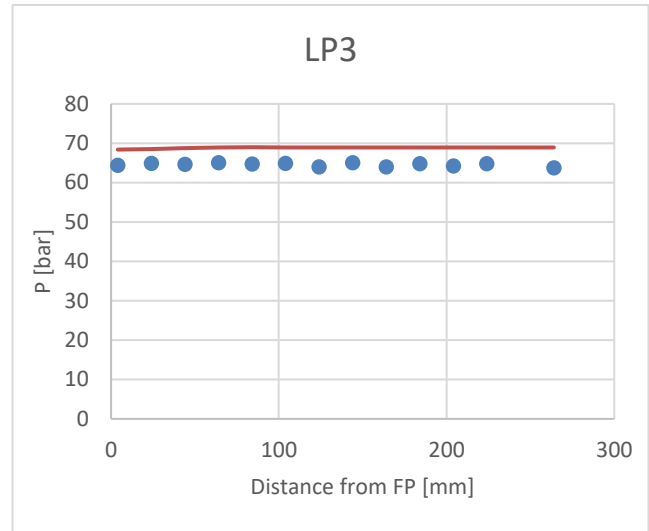
Figure 17: Measured (blue) and simulated (red) pressure levels at the walls for LP3
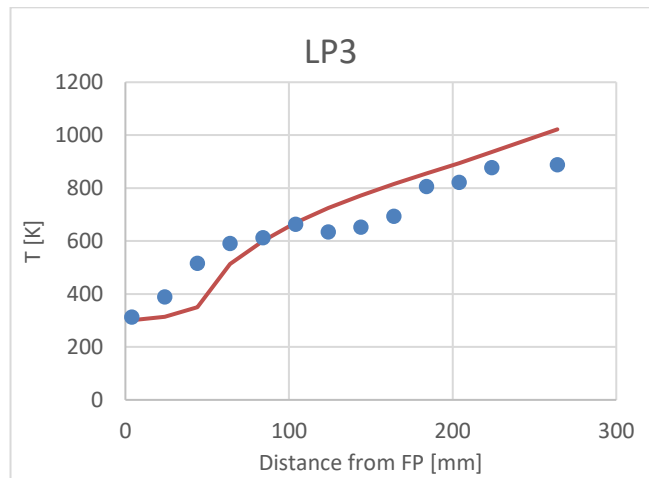
Figure 18: Measured (blue) and simulated (red) gas temperatures at the walls for LP3.

The agreement for the L1 mode of LP1 is poor, for reasons unknown, but it is likely to originate from the CFD solution since the characteristics of the mean flow field in the combustion chamber are the driving factor for the obtained acoustic frequencies in a CAA analysis. A chamber mode prediction for LP4 was not possible because the CFD solution did not converge. Both of these outcomes indicate the need for further development of the numerical tool to achieve reliable results. A further factor is the loss in resolution of stratification in the flow field when the CFD solution is interpolated onto the CAA domain, which has a coarser mesh to keep computational expense low. Short computational time is the primary advantage of using CAA for the acoustics.

The chamber frequencies are compared with the predicted LOX-post frequencies in Table 3. Mode coupling is predicted for LP2 and potentially LP3 due to the small frequency spacing. However, the L1-post values cannot be validated because no direct measurement of LOX-post frequency was available for those LPs from the experiment.

Table 2: Eigenfrequencies determined with Piano compared to experimental data. Error of numerical prediction is calculated from the relative difference of the two values.

[Hz]	L1 Piano	L1 exp	Error	L2 Piano	L2 Exp	Error
LP1	2670	2330-2430	10-14%	5118	4950	3.4%
LP2	2441	2380	2.6%	4959	4900	1.2%
LP3	2441	2350-2420	0.9-3.9%	4883	4910	-0.55%

Table 3: Comparison of calculated LOX-post and chamber eigenfrequencies.

[Hz]	L1 post	L1 chamber	Offset	L2 post	L2 chamber	Offset
LP1	2464	2670	-7.7%	5118	5136	-0.4%
LP2	2464	2441	0.9%	4959	5136	-3.4%
LP3	2474	2441	1.4%	4883	5159	-5.3%

3.3. CFD modelling

Both steady and unsteady CFD simulations of the BKN test case were performed by the Spacecraft Department of the DLR Institute of Aerodynamics and Flow Technology in Göttingen (DLR-AS). Two of the four LPs of the test case were addressed, namely LP3 and LP4. First, the steady flow field was calculated and compared to measured boundary conditions in the experiment. Then unsteady simulations were performed for comparison with the measured chamber acoustics and flame dynamic response.

All numerical simulations of BKN at DLR-AS were performed using the in-house TAU code. TAU is a 2nd order finite-volume code that employs a dual-cell approach for the spatial discretization. The numerical fluxes are calculated using the MAPS+ upwind scheme [27] which has been enhanced for accuracy and convergence properties in the low Mach number regime [28]. For time integration, TAU uses a three-stage Runge-Kutta scheme in combination with a local time-stepping approach for convergence acceleration. Time-accurate simulations are performed using a Jameson-type dual time stepping scheme with an unsteady time step size of 5×10^{-7} s.

Turbulence is considered using the Spalart-Allmaras turbulence model. More specifically, this work uses the standard SA model from the NASA turbulence modelling resource website [29]. Chemical reactions are included by using 6 species and 7 reaction detailed chemistry scheme of Gaffney [30]. In this method, the partial densities of all participating species (H_2, H, O_2, O, OH and H_2O) are transported by a separate conservation equation. The chemical source terms are calculated using a modified Arrhenius approach. The backward reaction rates are determined by dividing the equilibrium constant by the forward reaction rate. Due to the high combustion chamber pressure leading to near-equilibrium chemical reactions, the interaction between turbulence and chemical reactions is neglected.

The real gas properties of O_2 are included by using the cubic Soave-Redlich-Kwong equation of state [31]. All other species are treated as ideal gases.

Both 2D axisymmetric and 3D models were used. The 3D domain used half symmetry, as shown in Figure 19. Meshing of the injector are shown in Figure 20. All inflow boundaries of the 3D geometry are reoriented to account for axial injection. This applies to the main H_2 injector which is cut 46.5 mm upstream of the face plate. However, the sleeve-like dome structure connecting the inner and out H_2 injector is kept in the final mesh.
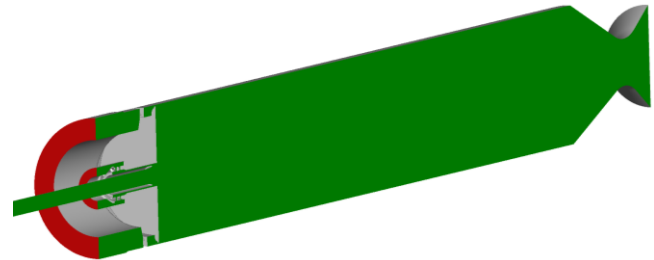
Figure 19: Mesh overview of the combustion chamber half domain including the symmetry boundary condition (green).
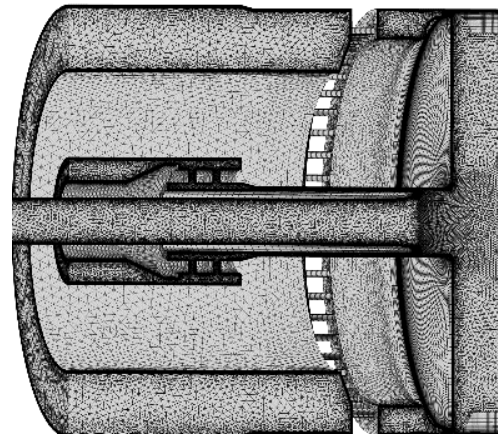
Figure 20: Mesh overview of the injector.

As a first step in this project, BKN is reduced to a 2D axisymmetric domain by extracting a slice of the full 3D geometry. The O_2 injector is cut at a length (inlet to injector

lip) of 48 mm. At the inlets, TAU uses a mass flux boundary condition at which the mass flux density and static temperature are prescribed. At the outlet, an exit-pressure outflow boundary condition is used.

The viscous (no-slip) walls in this setup can use different heat flux boundary conditions that will be compared later. All injectors walls, domes and the nozzle wall are treated as adiabatic walls. The combustion chamber walls are simulated using adiabatic walls, isothermal and a thermal-reservoir boundary condition. The reservoir temperature is taken as the structural temperature measured by thermocouples that are placed 1 mm below the combustion chamber surface.

3.4. Steady CFD results

This section provides the results of the steady simulations with TAU. It starts with an overview of the flame shape from the 2D simulation results and continues with a more detailed comparison with the experimental data.

The first results give a qualitative overview of the flame length and shape based on the temperature and the OH mass fraction. The temperature field, as well as the OH mass fraction field, indicate a longer flame shape for LP4 than LP3, as seen in Figure 21. This can be explained by the higher ROF for LP4 with 5.8 compared to 4 at LP3. As the total mass flux of O_2 and H_2 is almost the same for both load points, the different ROF causes a higher velocity in the O_2 injection that leads to a prolonged flame. Comparing the OH mass fraction flame shape in 2D in Figure 22 also shows a more pronounced flame shoulder region for LP4. The same effect is visible in the mean OH* radiation images from the experiments in Figure 9.

Several simulations were completed during the course of the project to investigate the steady state properties of BKN at LP3 and LP4. Different modelling strategies are applied to investigate the sensitivity and to find a suitable setup for the unsteady simulations. The model variations are

- 2D axisymmetric simulations with an adiabatic wall boundary condition
- 2D axisymmetric simulations with a thermal reservoir boundary condition (hereafter labelled as "th. res.")
- 3D half-model simulations with an adiabatic wall boundary condition
- 3D half-model simulations with a thermal reservoir boundary condition

The comparison of numerically predicted wall pressure and experimental measurements is shown in Figure 23. For LPs 3 and 4 we find a good agreement of the combustion chamber pressure, well within the experimental error bars. Between 100 mm and 250 mm, the experimental pressure is fluctuating between neighbouring sensors which is not represented in the numerical simulations. Especially for LP4

there is very little difference in combustion chamber pressure irrespective of the modelling strategy. From the pressure signals it is also evident that there is only a small influence of 2D modelling assumptions.
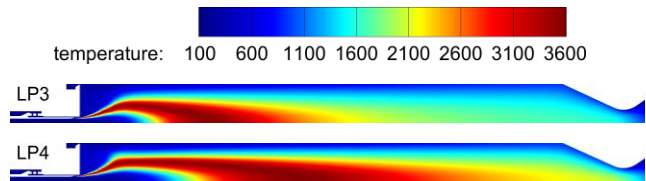
Figure 21: Comparison of the temperature field for LP3 and LP4.
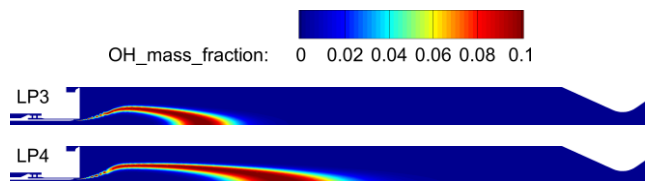
Figure 22: Comparison of the OH mass fraction field for LP3 and LP3.

While the agreement is good for the combustion chamber pressure, the wall temperature in the simulations shows significant deviations to the experimental data, as seen in Figure 24. Both wall boundary conditions (adiabatic and thermal reservoir) clearly underestimate the wall temperature for LP3 and even more strongly for LP4. This result is remarkable because the adiabatic wall temperature is an upper limit to the real wall temperature as it neglects any wall cooling effect. Presentation of simulation results with an isothermal wall boundary condition are omitted here as they give the correct wall temperature by design.

Another noteworthy aspect of all simulation results is the fact that the 2D simulations with thermal reservoir boundary condition differ only by a small amount from the 3D results (Figure 24) even though the window cooling geometry is strongly simplified in the 2D simulations.

All simulations with the thermal reservoir boundary condition predict a wall temperature that follows the trend of the experimental structural temperature. This is explained by the equation for the wall heat flux in which the structural temperature is used as the reservoir temperature of the boundary condition. The numerical wall temperature therefore follows the structural temperature which explains why the characteristic shape in the experiment, in particular the dip in wall temperature between 200 and 250 mm, is also seen in the wall temperature distribution.

3.5. Unsteady CFD results

In this Section the results of the unsteady modelling with TAU are presented. The first part of this section focusses on the determination of combustion chamber eigenmodes for

LP3 and LP4 using artificial pressure disturbances. The second part describes the results of continuous harmonic forcing of the inlet boundary conditions.

Starting from the steady-state RANS solutions shown before, we added localized pressure pulses to the stationary field and continued the simulation using the time accurate dual-time stepping scheme. These artificial pressure pulses then evolve in time and excite acoustic modes inside the combustion chamber. Chamber eigenmodes prevail for longer periods and vanish at a much lower damping rate than non-eigenmodes.
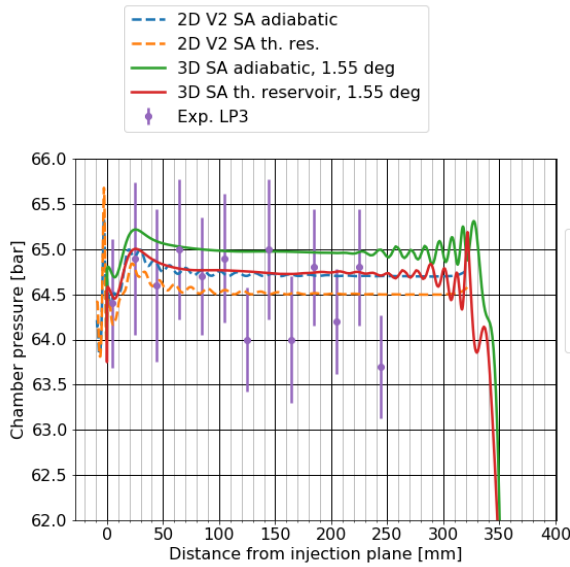

LP3
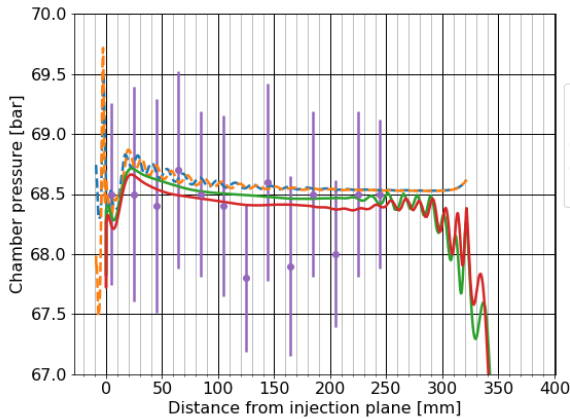
LP4

Figure 23: Comparison of pressure distributions

An exemplary result from the 3D simulation of LP4 is shown in Figure 25. A very pronounced peak is found in the PSD at around 5300 Hz corresponding to the 2L mode. DMD mode shapes can be retrieved from the unsteady surface data,

given in Figure 26 for LP4. Especially the 2L mode shows clearly pronounced nodal lines whose positions can be extracted for a further comparison to the experimental results.
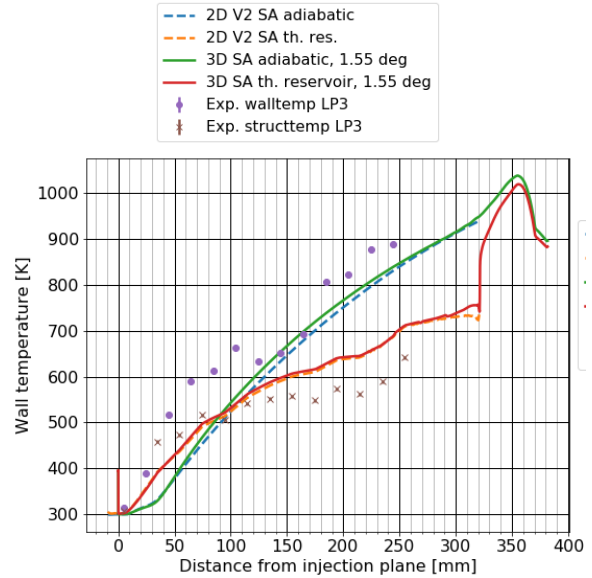
LP3
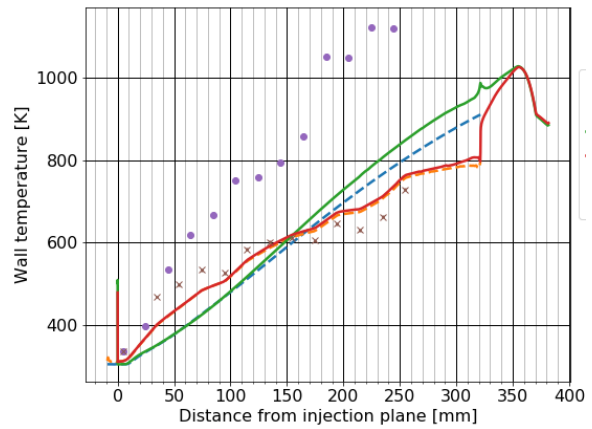
LP4

Figure 24: Comparison of wall temperature distributions

Table 4 compares the experimental and numerical eigenmode frequencies. One notices a consistent overestimation of the frequencies, especially for the 2L modes. For LP3, the 3D results show an even greater overestimation while for LP4, the 3D results for the 1L mode agree well with the experiment. The 2L frequency is very similar for the 2D and 3D simulations, though overestimated with respect to the experiment. The maximum deviation from the experiment is 12.7% for the LP3 1L mode. All other modes have an error of 10% or below.

The position of the nodal lines is well captured for the 1L and 2L modes of LP3. For LP4, the 3D simulation places the

1L nodal line 40 mm downstream of the experimental location. For the 2L mode, the position is reasonably well captured compared to the 1L mode.
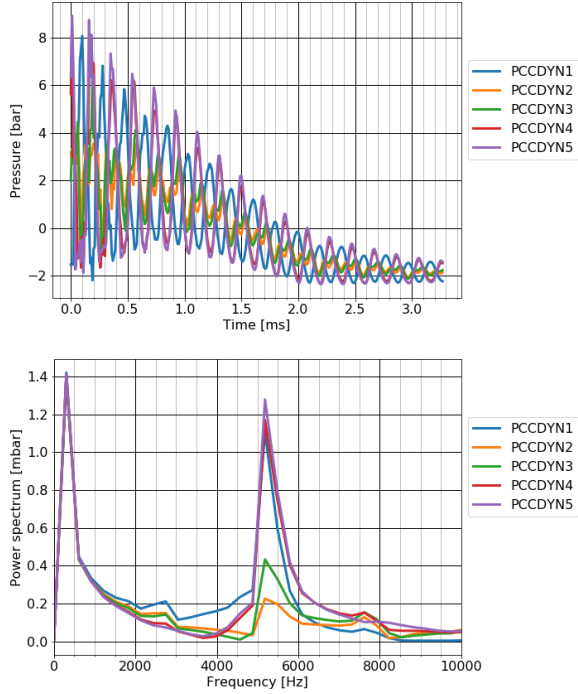
Figure 25: 3D bomb test pressure trace and chamber power spectrum for LP4
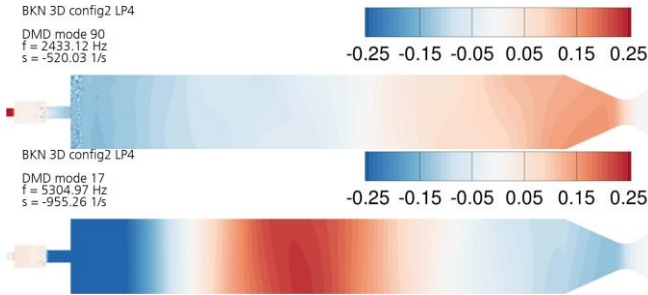
Figure 26: DMD mode shapes from the bombing test of LP4, showing the 1L mode (above), and 2L (below).

In order to investigate possible mechanism of combustion instability, we simulated LPs 3 and 4 with a continuously, harmonically excited mass flux oscillation at the inlet. We prescribed an oscillating mass flux of ±10% superimposed to the steady-state mass flux. The specific excitation frequencies were chosen based on the dominant eigenmode of the pressure response.

The result for LP3, with a mass flux excitation frequency set to 2580 Hz, is shown in Figure 27. After short transient phase of about 3 ms, the simulation responds with a limit cycle oscillation in the combustion chamber.

Table 4: Comparison of the experimental and numerical (from DMD results) eigenmode frequencies.

Mode	Load Point 3			Load Point 4		
	Exp. [Hz]	2D [Hz]	3D [Hz]	Exp. [Hz]	2D [Hz]	3D [Hz]
1L	2385	2583	2689	2430	2534	2433
2L	4910	5419	n/a	4960	5390	5304
3L	n/a	7896	7684	n/a	n/a	n/a

Table 5: Comparison of the experimental and numerical nodal line positions.

Mode	Load Point 3			Load Point 4		
	Exp. [mm]	2D [mm]	3D [mm]	Exp. [mm]	2D [mm]	3D [mm]
1L	161.8	155.5	158	154.5	147	187
2L	80.4 / 254.4	88 / 251	n/a	84.7 / 249.1	77 / 249	71 / 244

In order to investigate the gain resulting from the driven mass flux modulation, the Rayleigh index was calculated. Figure 28 shows normalised Rayleigh index iso-contours at ±0.1 integrated over one oscillation period and averaged over multiple oscillation cycles in the near-injector region. The contours describe the axisymmetric, pulsating response of the flame to the modulated in-flow. Note that locally the Rayleigh index can be negative while the integral over the combustion volume is always positive, indicating a net positive coupling between heat release and pressure oscillations.

3.6. Coupled injector-chamber simulation

LP3 was simulated again with the injector length adjusted to 61.0 mm to investigate the scenario where the combustion chamber 1L eigenmode at 2580 Hz and the injector 1L eigenmode at the same frequency are properly coupled.
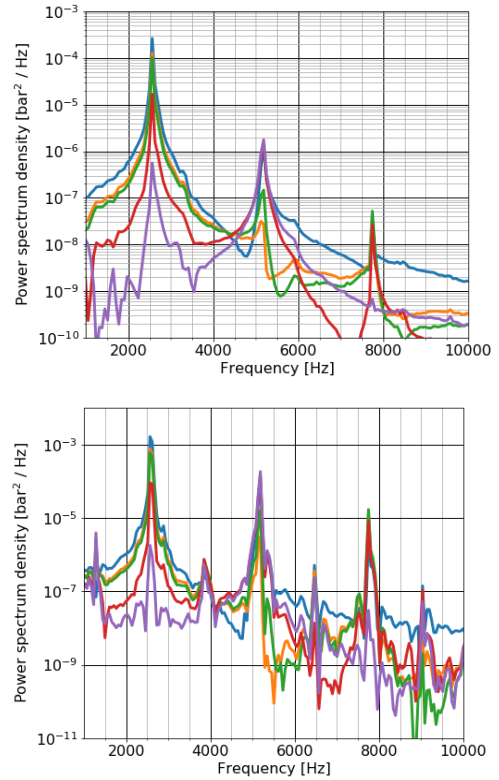
A comparison of the PSDs from pressure signals at various sensor locations is shown in Figure 29. These spectra, together with the RMS amplitude values in Table 6, show nearly an order of magnitude greater pressure response in both the combustion chamber and injector for the coupled case. This result emphasises the potential danger of injector-coupled combustion instabilities.

Table 6: Limit-cycle RMS pressure amplitudes for the coupled and uncoupled simulation.
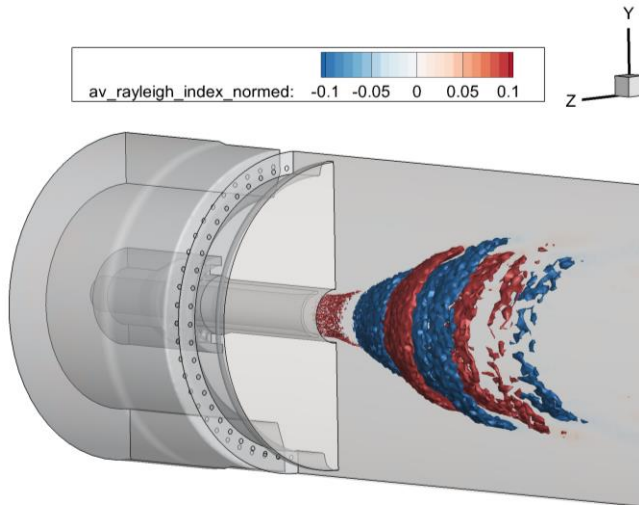
	Chamber Amplitude (PCCDYN1) p_{RMS} [bar]	Injector amplitude (LOX1) p_{RMS} [bar]	Ratio p_{inj}/p_c
Decoupled	0.085	4.9	57.6
Coupled	0.29	15.0	51.7
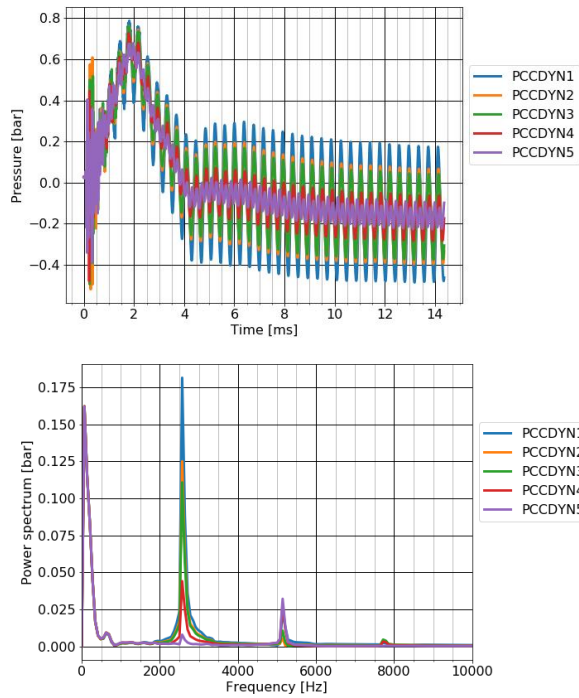
**Figure 27: Simulation of LP3 continuous inflow oxygen mass flux oscillations.**

Figure 28: Normalized Rayleigh index iso contours at ± 0.1 integrated over one oscillation period and averaged over multiple oscillation cycles.

Figure 29: Combustion chamber pressure PSDs from uncoupled (above) and coupled (below) LP3 simulations.

The mode distributions of the four dominant modes were extracted with DMD and are shown in Figure 30. For each frequency the chamber mode is shown above and a zoomed view of the LOX post below. The distributions show that some injector modes resemble a simple closed-open organ pipe mode with a velocity antinode at the outlet, while others take the form of a mode with closed-closed boundary conditions and a pressure antinode at the outlet to the combustion chamber. This result indicates that the simple pipe-mode model oversimplifies the true situation at the junction between injector and combustion chamber. This virtual interface can support both types of acoustic boundary conditions (acoustically open vs. closed), and both types can couple with compatible combustion chamber modes simultaneously.

f = 2579.4 Hz

f = 5158.5 Hz

f = 6451.0 Hz

f = 7737.7 Hz
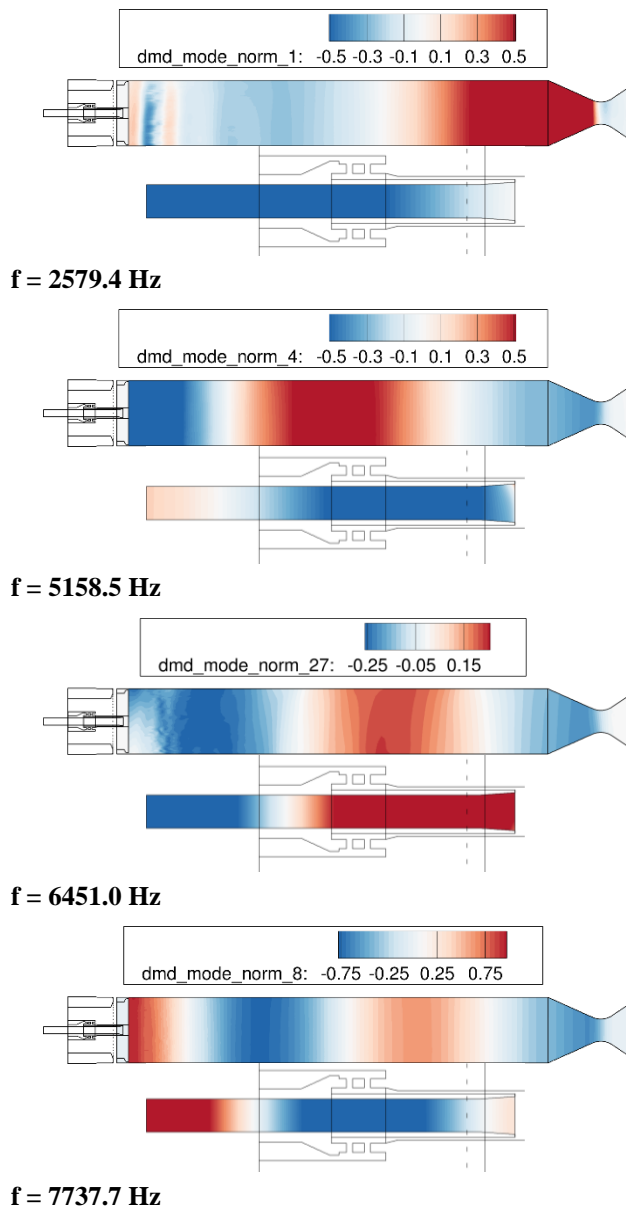
Figure 30: DMD mode shapes from the coupled injector simulation at dominant frequencies showing chamber (above) and zoomed injector (below).

4.   SUMMARY AND OUTLOOK

A new, high-pressure, cryogenic, rocket combustion experiment which has the potential to serve as a landmark test case for validating numerical tools was inaugurated. The configuration was well suited for the subsequent numerical modelling which sought to recover its stability behaviour, and the modelling resulted in new insights into the injection coupling phenomenon.

Although highly limited in scope, and utilising a hitherto untested injector element and innovative combustion chamber design, the experiments at the P8 Test Facility resulted in coherent data sets for seven different operating conditions, or 'load points' (LPs). The flame characteristics for all seven LPs could be analysed from high-speed imaging, and a wider flame opening angle for higher momentum flux ratios was observed.

Even though no sign of LOX post coupling was visible in the pressure sensors, precise identification of dynamic flame response originating from the LOX injector was possible from the analysis of the imaging. It was the imaging analysis which confirmed the spacing between injector and chamber frequencies and therefore explained the absence of strong coupling, precluding self-excitation to high acoustic amplitudes.

The experimental data was used to define a test case to assess the accuracy of numerical modelling tools. This task served as a reminder that modelling high-pressure cryogenic combustion is still a challenge. Characteristics such as strong thermodynamic property gradients, flow field stratification, and order-of-magnitude difference in geometrical scale between injector and chamber pose challenges to all state-of-the-art modelling approaches.

The test case was in general well suited to assess tool performance in light of these challenges. The scale of the combustor was manageable with all tools and could be addressed as a full 3D configuration. The availability of data from the BKN experiment was positively received by the modellers. The large optical-access windows provided world-leading imaging of the flame for comparison with CFD results. The distributed temperature measurements at the wall could be utilised to define a thermal boundary condition in the CFD models. The extensive array of high frequency pressure sensors allowed not only the frequency but also the pressure distribution or position of the nodal line of acoustic eigenmodes to serve as validation data.

A drawback of the experiment was the lack of self-excitation of LOX-post modes which hindered identification of their frequencies as a source of validation data and negated the study of high amplitude flame dynamics. Achieving high acoustic amplitudes should receive high priority for future experimental work, and be accompanied by numerical modelling.

The hybrid CFD-CAA approach to predicting injector coupling performed satisfactorily with a relatively coarse mesh for the acoustic calculations and correspondingly low computational expense. A course mesh in the CAA computational domain necessitated artificial reduction in the property stratification, and so any related effect was not resolved. Numerical expense would increase exponentially with an attempt to resolve these effects with the PIANO solver, in which case resolving acoustic perturbations in an unsteady CFD simulation becomes the preferable option. The

computational expense of using CFD is an order of magnitude higher, but stratification effects are in that case resolved in the computational domain, as well as the re-distribution of acoustic properties resulting from the flame acoustic response, which is particularly important if transverse-mode instabilities are to be addressed in a full-scale thrust chamber configuration.

CFD modelling using the TAU solver successfully provided steady-state and unsteady RANS results for two supercritical load points of BKN. While the overall agreement for the chamber pressure was very good, there were differences between the experimental and the numerical wall temperature distribution. Further validation studies could include a more detailed model of the wall heat transfer as this aspect of the simulation currently has the highest uncertainty.

Numerical bombing tests successfully provided the dominant chamber eigenmodes and their frequencies with a maximum error of 13.7%. High damping of longitudinal modes reduced the frequency resolution of this method to some degree but still provided results sufficient for comparison with experiment. Averaging the timeseries of multiple virtual bombing tests is expected give better spectral statistics and thereby a better estimate of the eigenmode frequencies.

Unsteady simulations with a forced inflow modulation at the LOX-post inlet provided insight into the mechanisms of injector coupling and showed a significantly increased pressure amplitude for the modified injector length that permitted resonant coupling. A detailed analysis of the injector and chamber modes also indicate that only certain chamber and injector modes can be coupled. These results, together with the experienced gained in running-in the new experiment, would allow targeted refinement of the injector geometry to greatly increase the certainty of injector coupling in future BKN testing.

5. ACKNOWLEDGEMENTS

6. REFERENCES

[1] W. S. Tomazic, E. W. Conrad and T. W. Godwin, "M-1 injector development - philosophy and implementation," *Journal of Spacecraft,* pp. vol.5, no.3, pp. 282-287, 1968.

[2] V. Yang and W. E. Anderson, Liquid rocket engine combustion instability, Progress in Aeronautics and Astronautics, vol. 169, Washington D.C.: AIAA, 1995.

[3] D. Watanabe, T. Tamura, T. Onga, H. Manako, N. Negoro, A. Kurosu, T. Kobayashi and K. Okita, "Hot-fire Testing of LE-X Thrust Chamber Assembly," in *30th International Space Transportation Symposium*, Kobe, Japan, 2015.

[4] D. Watanabe, "Hot-fire Testing of Development Booster Engine for H3 Launch Vehicle," in *Space Propulsion Conference*, Rome, 2016.

[5] J. P. Wanhainen, H. C. Parish and E. W. Conrad, "Effect of propellant injection velocity on screech in a 20 000-pound hydrogen-oxygen rocket engine, TN D-3373," NASA, 1966.

[6] H. E. Scott, H. E. Bloomer and A. H. Mansour, "M-1 Engine Subscale Injector Tests," NASA, 1967.

[7] W. F. Dankhoff, I. A. Johnson, W. Conrad and W. A. Tomazic, "M-1 Injector Development - Philosophy and Implementation," NASA, 1968.

[8] E. W. Conrad, H. E. Bloomer, J. P. Wanhainen and D. W. Vincent, "Interim summary of liquid rocket acoustic-mode-instability studies at a nominal thrust of 20 000 pounds, TN D-4968," NASA, 1968.

[9] N. P. Hannum and E. W. Conrad, "Performance and screech characteristics of a series of 2500-pound-thrust-per-element injectors for a liquid-oxygen-hydrogen rocket engine, TM X-1253," NASA, 1966.

[10] R. Salmi, J. Wanhainen and N. Hannun, "Effect of Thrust per Element on Combustion Stability Characteristics of Hydrogen-Oxygen Rocket Engines," NASA, 1968.

[11] J. P. Wanhainen, C. E. Feiler and C. J. Morgan, "Effect of chamber pressure, flow per element, and contraction ratio on acoustic-mode instability in hydrogen-oxygen rockets, TN D-4851," NASA, 1968.

[12] J. P. Wanhainen, N. P. Hannum and L. M. Russell, "Evaluation of screech suppression concepts in a 20 000-pound-thrust-hydrogen-oxygen rocket, TM X-1435," NASA, 1967.

[13] J. P. Wanhainen and C. J. Morgan, "Effect of injection element radial distribution and chamber geometry on acoustic-mode instability in a hydrogen oxygen rocket, TN D-5375," NASA, 1969.

[14] DLR, "DLR-LA-HF-RP-064-ASTG: Battleship combustor for unsteady combustion process analysis, Logic for further work, ESA contract 4000104621/11/NL/RA," DLR, Lampoldshausen, 2012.

[15] S. Gröning, D. Suslov, J. Hardi and M. Oschwald, "Influence of Hydrogen Temperature on the Acoustics

of a Rocket Engine Combustion Chamber Operated with LOX/H2 at Representative Conditions," in *Space Propulsion 2014*, Paris, 2014.

[16] S. Gröning, J. Hardi, D. Suslov and M. Oschwald, "Influence of hydrogen temperature on the stability of a rocket engine combustor operated with hydrogen and oxygen," *CEAS Space Journal,* vol. accepted for publication, 2016.

[17] S. Gröning, J. S. Hardi, D. Suslov and M. Oschwald, "Injector-Driven Combustion Instabilities in a Hydrogen/Oxygen rocket combustor," *Journal of Propulsion and Power,* pp. vol.32, no.3, pp.560-573, 2016.

[18] J. Hardi, F. Tonti, W. Armbruster, P. N. Blanco, R. Kaess, T. Horchler and S. Karl, "TN1100 Final study report - ESA TRP | Coupling mechanisms of combustion and acoustics in rocket combustors | ESA-IPL-PTM-SFe-st-LE-2015-510," DLR Institute of Space Propulsion, Lampoldshausen, Germany, 2017.

[19] DLR, "DLR-LA-HF-RP-089: TN1100 Final study report," DLR, Lampoldshausen, 2017.

[20] J. Martin, W. Armbruster, R. Stützer, S. General, B. Knapp, D. Suslov and J. Hardi, "Flame characteristics of a high-pressure LOX/H2 rocket combustor with large optical access," *Case Studies in Thermal Engineering,* vol. 28, no. 101546, 2021.

[21] T. Fiala, "Radiation from high pressure hydrogen-oxygen flames and its use in assessing rocket combustion instability," Technical University Munich, Munich, Germany, 2015.

[22] T. Fiala, S. Gröning, T. Sattelmayer, J. Hardi, R. Stützer, S. Webster and M. Oschwald, "Comparison Between Excited Hydroxyl Radical and Blue Radiation from Hydrogen Rocket Combustion," *Journal of Propulsion and Power,* pp. 490-500, 2017.

[23] D. Kendrick, G. S. C. Herding, C. Rolon and S. Candel, "Effects of a Recess on Cryogenic Flame Stabilization," *Combustion and Flame,* pp. 327-339, 1999.

[24] W. Armbruster, J. Hardi and M. Oschwald, "Impact of shear-coaxial injector hydrodynamics on high-frequency combustion instabilities in a representative cryogenic rocket engine," in *Symposium on Thermoacoustics in Combustion: Industry meets Academia (SoTiC 2021)*, Munich, 2021.

[25] P. Schmid, "Dynamic mode decomposition of numerical and experimental data," *Journal of Fluid Mechanics,* p. 5–28, 2010.

[26] S. K. Beinke, "Anaylses of Flame Response to Acoustic Forcing," School of Mechanical Engineering, The University of Adelaide, Australia, 2017.

[27] C.-C. Rossow, "Extension of a compressible code toward the incompressible limit," *AIAA journal,* vol. 41, no. 12, pp. 2379-2386, 2003.

[28] B. Thornber, A. Mosedale, D. Drikakis, D. Youngs and R. Williams, "An improved reconstruction method for compressible flows with low Mach number features," *Journal of Computational Physics,* vol. 227, no. 10, pp. 4873-4894, 2008.

[29] C. Rumsey, *Turbulence Modeling Resource.*

[30] R. Gaffney Jr, J. White, S. Girimaji and J. Drummond, "Modeling turbulent/chemistry interactions using assumed PDF methods," in *Joint Propulsion Conference and Exhibit*, 1992.

[31] S.-K. Kim, H.-S. Choi and Y. Kim, "Thermodynamic modeling based on a generalized cubic equation of state for kerosene/LOx rocket combustion," *Combustion and flame,* vol. 159, no. 3, pp. 1351-1365, 2012.